Thin Solid Films 709 (2020) 138245

Contents lists available at ScienceDirect

Thin Solid Films

journal homepage: www.elsevier.com/locate/tsf

Al incorporation during metal organic chemical vapour deposition of aluminium zinc oxide

Josef Ellingsen[a,*], Vishnukanthan Venkatachalapathy[a,c], Alexander Azarov[a], Ola Nilsen[b], Andrej Kuznetsov[a]

[a] LENS, Department of Physics, University of Oslo, Blindern, PO Box 1048, Oslo 0316, Norway
[b] NAFUMA, Department of Chemistry, University of Oslo, Blindern, PO Box 1033, Oslo 0315, Norway
[c] Department of Materials Science, National Research Nuclear University MEPhI, 31 Kashirskoe sh, Moscow, Russia

ARTICLE INFO

Keywords:
Thin films
Metal-organic chemical vapor deposition
Growth conditions
Boundary layer
Doping
Compound semiconductors
Aluminum-doped zinc oxide (TSF scientific staff)

ABSTRACT

Aluminium zinc oxide (AZO) is a promising transparent conductive oxide this is difficult to fabricate by metal-organic chemical vapour deposition (MOCVD) because of prereactions between the precursors for Al and oxygen. One way of reducing prereactions is to use separate injectors. In this work, we investigated the effect of separate injectors and various flow configurations on the MOCVD fabrication of AZO using diethyl zinc (DEZn), tert-butanol (tBuOH), and trimethyl aluminium (TMAl) precursors.

X-ray diffraction revealed that the resulting films maintained a purely wurtzite ZnO structure, and that the Al incorporation changed the c lattice parameters from 5.207 to 5.181 Å in agreement with theoretical models of mixing on the Zn sub-lattice. This indicates that Al was mainly incorporated onto the Zn sub-lattice. The maximum Al concentration was 6×10^{21} cm^{-3}.

The Al concentration was directly influenced by the TMAl flow rates, but the incorporation efficiency of Al also depended on the O/Zn balance as determined by the tBuOH supply and the total flow rate through the TMAl +DEZn injector. The tBuOH supply decreased the incorporation efficiency, while it increased for higher total flow in the TMAl+DEZn injector although both changes nominally increases the O/Zn balance. This dual, but contradicting, dependency on the O/Zn suggested that the incorporation efficiency depended not only on precursor supply, but also on the chemical stability of the Al species present at the growth interface. The concept of a reaction depth of TMAl was introduced to discuss the observed trends, and a qualitative model was suggested to explain how the Al-species present at the growth interface are determined by the relative depths of the reaction depth and the boundary layer. These findings illustrate the limits of the O/Zn parameter when using separate injectors because the properties of the boundary layer can affect Al incorporation during MOCVD growth. This should be relevant for MOCVD growth of other compound semiconductor systems that are grown using separate injectors.

1. Introduction

Aluminium zinc oxide (AZO) is a popular transparent conductive oxide (TCO) whose applications include photovoltaics [1], light emitting diodes [2,3], smart-windows, Minami [4], resistive switching in memristors [5,6], and optical switching in nanophotonics [7]. The optical and electrical properties of AZO as a TCO are comparable to those of indium-tin oxide (ITO), which is the industry standard. AZO is a contender to be a cheaper and more environmentally friendly alternative to ITO because aluminium and zinc are more abundant than indium [8].

AZO can be fabricated through several methods such as sputtering, Minami et al. [9], Sernelius et al. [10], Liu et al. [11] spray pyrolysis, Hung-Chun Lai et al. [12], Nakrela et al. [13] pulsed laser deposition, Cao et al. [14], Coman et al. [15], Park et al. [16], atomic layer deposition (ALD), Dasgupta et al. [17], Lee et al. [18], Tynell et al. [19], Elam and George [20] metal-organic chemical vapour deposition (MOCVD), Hu and Gordon [21], Kuprenaite et al. [22], Brochen et al. [23] and mist-CVD [24]. MOCVD is a particularly interesting growth method because it is well suited for industrial scaling and can produce abrupt films with excellent composition control and high growth rates. High quality ZnO has been grown by MOCVD using diethyl zinc (DEZn,

* Corresponding author.
E-mail address: j.g.a.ellingsen@fys.uio.no (J. Ellingsen).

https://doi.org/10.1016/j.tsf.2020.138245
Received 20 November 2019; Received in revised form 17 July 2020; Accepted 20 July 2020
Available online 21 July 2020
0040-6090/ © 2020 The Authors. Published by Elsevier B.V. This is an open access article under the CC BY license (http://creativecommons.org/licenses/BY/4.0/).

$(C_2H_5)_2Zn$) and alcohols such as tert-butanol (tBuOH, $(CH_3)_3COH$) [25,26]. This growth process is normally explained in terms of DEZn combining with tBuOH to form an alkyl zinc alkoxide adduct that decomposes at the growth interface [25,27]. However, Al incorporation during ZnO growth is challenging because the most common Al precursors used in MOCVD, such as trimethyl aluminium (TMAl, $Al(CH_3)_3$) [27,28] and triethyl aluminium(TEA, $Al(C_2H_5)_3$) [21], are very reactive in the presence of oxygen precursors because of an unfilled *p*-orbital on the Al atom.

Less reactive precursors such as aluminium acetate have been used to make AZO by mist-CVD [24] or aerosol-assisted MOCVD, Kuprenaite et al. [22]. However, prereactions when using TMAl or TEA have been reduced by configuring the MOCVD with separate injectors for metal-organic and oxygen precursors [21,28–30]. Cleverly separated injectors prevent the reactive precursors from meeting until they are closer to the growth interface. In the best case scenario, separate injectors will confine gas phase reactions of the precursors entirely to the gas diffusion boundary layer. The importance of the boundary layer to dopant incorporation and film growth is implicitly understood, but little or nothing is known about how flow rates and reactions in the boundary layer affect impurity incorporation when using separate injectors.

In the current work, we have fabricated AZO using some very common precursors, namely DEZn, tBuOH and TMAl, in an MOCVD reactor with separate injectors for oxygen and metal-organic precursors. By applying various flow configuration, we have investigated the effects of oxygen to zinc ratio (O/Zn) and the boundary layer thickness on Al incorporation during MOCVD growth.

2. Methods

2.1. Fabrication

AZO films with thicknesses of 200 nm–400 nm were deposited on C-oriented α-Al_2O_3 in an EMF Titan MOCVD using diethyl zinc (DEZn, CamChem VR grade) and trimethyl aluminium (TMAl, CamChem DEOX grade) as precursors for Zn and Al, respectively. Tert-butanol (t-BuOH, Sigma-Aldrich anhydrous, 99.5%) was used as an oxygen precursor. The carrier gas was purified nitrogen, N_2. Prior to deposition, the substrates were cleaned with acetone and ethanol in an ultrasonic bath, followed by treatment in a piranha solution(H_2SO_4:H_2O_2:H_2O (1:1:6)). After loading the substrates into the reactor, they were heat-treated at 700 °C for 20 min in N_2. The substrates were then cooled to the growth temperature in preparation for the start of the growth process. The growth temperature was 370 °C and the pressure was kept at 80 kPa, following conditions previously optimized for ZnO growth [31]. The MOCVD design featured separate line injectors for tBuOH and TMAl + DEZn as illustrated in Fig. 1 [32]. The molar flow rates of the precursors, Q_{prec}, were estimated using Eq. (1).

$$Q_{prec} = \frac{F_{prec}}{V_{STP}} \times \frac{p_{prec}}{P_{bub} - p_{prec}} \ (\text{mol min}^{-1}) \tag{1}$$

where *prec* is either TMAl, tBuOH, or DEZn. F_{prec} is the bubbler flow in sccm. p_{prec} is the partial pressure of the precursor, P_{bub} and T are the total pressure in the bubbler, and the bubbler temperature, respectively. V_{STP} is the volume of one mole of ideal gas at standard pressure and temperature (101 kPa and 300 K), and has an approximate value of 22400 cm^3 mol^{-1}. The flow rate from each bubbler was diluted in N_2 to produce a total flow rate of 1000 sccm. Additional carrier/push flows were applied to each line separately, and the flows were directed over a rotating sample holder. The exhausts, marked by large arrows, ensured that the flows did not mix. The sample holder rotated at 60 rpm and alternately exposed the substrates to the metal-organic (MO) mixture (DEZn + TMAl) and tBuOH. Reactions between DEZn + TMAl and tBuOH were thus confined to the diffusion boundary layer.

The flow conditions used for the AZO deposition were systematically varied by changing one flow parameter at a time. The volumetric flow rates used are summarized in Table 1. The series in Table 1 are labelled TMAl, tBuOH, MO150, MO175, and MO200 according to the flow rate that was varied. For each of the MOxxx series, the tBuOH flow rate was kept constant at xxx sccm. The flow rate to the DEZn bubbler, F_{DEZn}, was kept constant at 100 sccm. While the tBuOH bubbler flow was varied, the total flow in the tBuOH injector, F_{TOT}^{tBuOH}, was kept constant at 7000 sccm. The oxygen to zinc ratio (O/Zn) in the boundary layer was calculated using Eq. (2), which was derived by combining Eq. (1) with the ideal gas law. The gas molar fraction, x_v was calculated using the molar flows of TMAl and DEZn, as in Eq. (3)

$$O/Zn = \frac{Q_{tBuOH}}{Q_{DEZn}} \times \frac{F_{TOT}^{MO}}{F_{TOT}^{tBuOH}} \tag{2}$$

$$x_v = Q_{TMAl}/(Q_{TMAl} + Q_{DEZn}) \tag{3}$$

2.2. Reactions

The reaction between DEZn and tBuOH during MOCVD growth involves the formation of an adduct or intermediary product, as shown in Eq. (4) [33]. At 370 °C, tBuOH is partially decomposed into isobutene and water, Thiandoume et al. [34], which facilitates for the reaction in Eq. (5). Growth occurs when the products of Eqs. (4) and (5) decompose at the surface [33], which can be described by Eq. (6). The resulting surface after decomposition will most likely be terminated by |-OR, where R = Et (C_2H_5) or H.

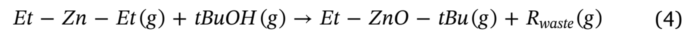

$$Et - Zn - Et(g) + tBuOH(g) \rightarrow Et - ZnO - tBu(g) + R_{waste}(g) \tag{4}$$

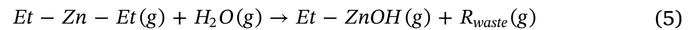

$$Et - Zn - Et(g) + H_2O(g) \rightarrow Et - ZnOH(g) + R_{waste}(g) \tag{5}$$

$$| - OR'(s) + Et - ZnOR(g) \rightarrow | - OZn - OR(s) + R_{waste}(g) \tag{6}$$

Here, Et and tBu refer to ethyl (C_2H_5) and tertiary-butyl $(CH_3)_3C$,

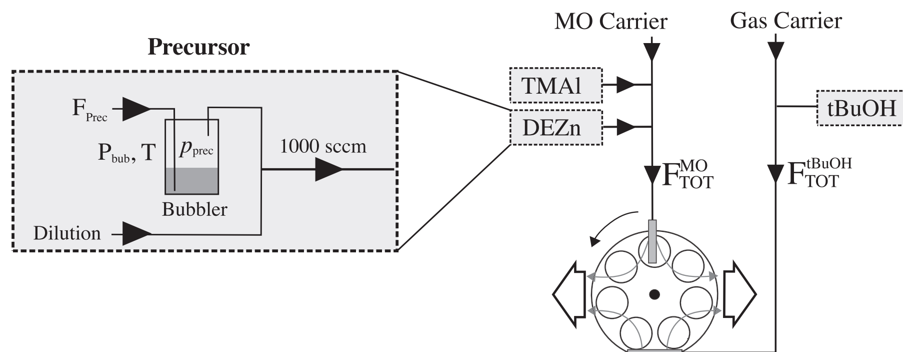

Fig. 1. The MOCVD reactor used in this work had separate injectors for precursor flows of tBuOH and DEZn + TMAl, and directed the flows over a rotating sample holder. The exhausts, marked by large arrows, ensured that the flows did not mix, and that mixing of the precursors were confined to the boundary layer.

respectively. R and R' can be either H or Et, and R_{waste} is some organic waste molecule such as butene or ethane. |– denotes the crystal surface.

2.3. Characterization

The chemical contents of Al in the films were measured by secondary ion mass spectrometry (SIMS). Signals from ^{64}Zn and ^{27}Al isotopes were recorded and the primary sputtering beam consisted of O^{2+}, with a raster size of 150 µm. The Al signals were converted into nominal concentrations by calibrating against an Al-implanted ZnO reference sample with a peak Al concentration of 6×10^{18} cm^{-3}. The uncertainty of this method is nominally within 10% for concentrations of a similar order, but may be larger for much higher Al concentrations because the sputtering efficiency may change. The depth of the sputtered craters were measured using a Dektak 8 profilometer, and the sputtering rates were assumed to be constant throughout the film. Al content in $Al_xZn_{1-x}O$ was given by $x = Al/(Al+Zn)$, where, the Al concentration was obtained from SIMS and Al + Zn was estimated from the theoretical density of Zn sites to be 4.2×10^{22} cm^{-3}. The structural properties of the thin films were investigated by X-ray diffraction (XRD) using $\omega - 2\theta$ scans. The scans were obtained on a Bruker D8 X-ray diffractometer using a CuK source and Goebel mirrors. The CuK-α1 contribution was isolated by fitting the peaks using two PseudoVoigt functions with relative amplitudes corresponding to those of CuK-α1 and CuK-α2. The (006) peak of α-Al_2O_3 was set to 41.676 ° for all samples to provide a standard for the shift of the peaks. The lattice parameters were obtained from the lattice spacing by Eq. (7).

$$\frac{1}{d^2} = \frac{l^2}{c^2} + \frac{4}{3}\left(\frac{h^2 + hk + k^2}{a^2}\right) \tag{7}$$

where *hkl* are the Miller indices, and *d*, *a*, and *c* were, respectively, the lattice spacing and the hexagonal lattice parameters of the crystal. The lattice spacings, *d*, were extracted from the (002) and (110) XRD peaks using Bragg's law. The full width at half maximum (FWHM) and peak locations were extracted from the fitted models, and grain sizes were estimated using Scherrer's equation, $D = 0.9\lambda/(FWHM_{002}\cos\theta)$, Holzwarth and Gibson [35] where λ was 1.506 Å, $FWHM_{002}$ was the FWHM of the 002 diffraction peak, and θ was the diffraction angle. The samples were also investigated using scanning electron microscope, but no surface structure was observed, confirming that grain sizes were smaller than the resolution of the equipment at 10,000X magnification. Electrical resistivity, Hall mobility, and carrier density were measured at room temperature with a four point probe and by Hall effect measurements in the van der Pauw geometry under room temperature. Transmission measurements were obtained by using a Shimadzu SolidSpec-3700 DUV spectrophotometer with an integrating sphere.

3. Results and discussion

3.1. Al concentration

The SIMS profile of a representative sample (20 sccm TMAl flow) is shown in the inset of Fig. 2. This profile demonstrates a sharp rise in Al concentration near the surface, followed by a flat region, a shoulder and a sharp drop where the film meets the substrate. The location of the substrate gives an estimate of the thickness of the film. The increased signal near the surface can be attributed to two factors. Firstly, it may reflect an increased sputtering efficiency at the surface because the sputtering and ionization processes have not yet reached a steady state. Secondly, it may reflect actually higher Al concentrations caused by a high mixing energy in the solid state, which cause impurity segregation. Impurities tend to build up near the growth surface because this is associated with less strain energy. This mechanism explains the shoulder in the profile near the substrate, and is described in detail by Greene et al. [36]. The Al concentration of each sample was therefore estimated

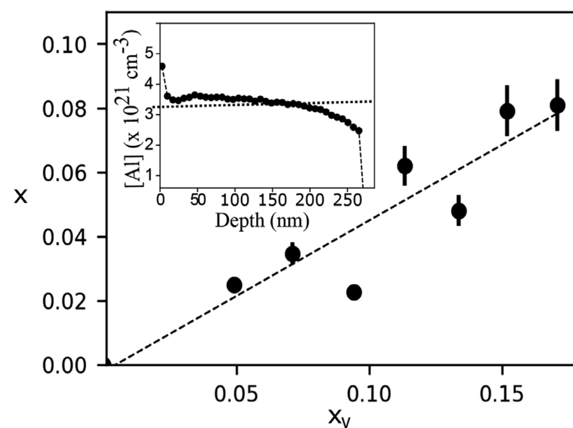

Fig. 2. $x = Al/(Al+Zn)$, is shown as a function of the gas molar fraction, $x_v = Q_{TMAl}/(Q_{TMAl} + Q_{DEZn})$. x_v was varied by increasing the TMAl supply in the the MO injector according to the TMAl series in Table 1. Insert: The SIMS profile a representative AZO sample. The Al concentration is estimated from the flat region indicated by the dotted line.

Table 1
The table shows the flow combinations used in the fabrication of each sample series. F_{TMAl} and F_{tBuOH} refer to the bubbler flow rates for TMAl and tBuOH, respectively. F^{MO}_{TOT} is the total volumetric flow rate coming through the MO injector, and is increased by using higher MO carrier flow rates. The flow rates were varied in steps of 2.5 sccm, 25 sccm, and 500 sccm for F_{TMAl}, F_{tBuOH}, and F^{MO}_{TOT}, respectively.

	Flow rates (sccm)		
Series	F_{TMAl}	F_{tBuOH}	F^{MO}_{TOT}
TMAl	**5–20**	150	3500
tBuOH	10	**75–200**	5500
MO150	10	150	**3500–5500**
MO175	10	175	**3500–5500**
MO200	10	200	**3500–5500**

by the flat region, as marked by the dotted line, which corresponds to the bulk concentration. The Al concentrations in the films range from 1×10^{17} cm^{-3} ($x = 0.00$) for pure ZnO to a maximum concentration of 6×10^{21} cm^{-3} ($x = 0.14$).

Fig. 2 also shows the relationship between the gas molar fraction of TMAl, $x_v = Q_{TMAl}/(Q_{TMAl} + Q_{DEZn})$ and x, as the TMAl flow is increased from 5 sccm to 20 sccm. x appears to depend on x_v in a linear fashion in this range. Impurity incorporation is sometimes discussed in terms of an incorporation efficiency, also called distribution coefficient [37]. The incorporation efficiency can be defined as $k = x/x_v$. The linear trend in Fig. 2 corresponds to an incorporation efficiency of $k = 0.5 \pm 0.1$. This means that the concentrations of Al in these films are roughly half the concentrations of TMAl in the gas phase during growth.

3.2. Structural properties

Fig. 3 shows two representative XRD profiles for ZnO and AZO. The ZnO film is preferentially oriented along the [001] direction as demonstrated by a single peak at 34.42 °, corresponding to the expected reflections of the (002) planes. Peaks at 41.68 ° and 72.57 ° correspond to the C-oriented α-Al_2O_3 substrate and the second order peak of the (002) planes in ZnO, respectively. The grain size estimated from applying Scherrer's equation to the FWHM of the (002) peak is ~ 120 nm. The AZO sample demonstrate a similar structure, but with a broadening of the (002) peak shape, and a shift of the peak location to 34.54 °. The AZO profile also demonstrates additional peaks at 32.02 °, 36.41 °, and 57.04 °. Incorporating Al into ZnO often leads to the formation of

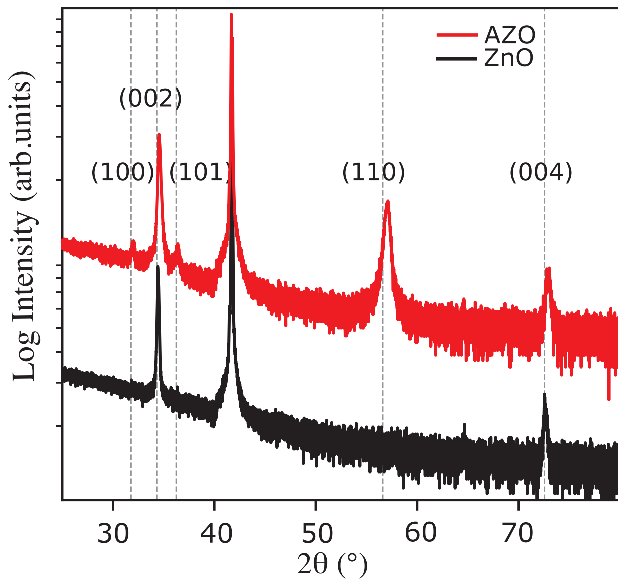

Fig. 3. The figure shows XRD profiles of pure ZnO (black) and a representative sample of AZO (red). Vertical lines mark the expected reflections of the ZnO wurtzite structure, with Miller's indices given. The unmarked peak at 41.68 ° is from the (006) planes of the α-Al_2O_3 substrate. The sample peaks are consistent with the wurtzite structure. (For interpretation of the references to color in this figure legend, the reader is referred to the web version of this article.)

$ZnAl_2O_4$, [38] which has reflections located at 31.25 °, 36.83 °, and 55.62 °, corresponding to spinel planes (220), (311), (422), respectively. However, the lattice parameters extracted from the measured AZO reflections, using Eq. (7) are perfectly consistent with the wurtzite structure. It is therefore reasonable to conclude that the films are all purely wurtzite phase with no detectable secondary phases. The broadening of the (002) reflection indicates that the grain sizes were reduced to about ~ 60 nm. This may be a result of strain at the grain boundaries introduced by concentration gradients of Al within the grains. The presence of (100), (101), and (110) planes in the film may have resulted from the relaxation of strain these strains.

The *c* and *a* lattice parameters of AZO are plotted in Fig. 4 as a function of x = Al/(Al+Zn). The data points in Fig. 4 show that *c* and *a* both decreased with greater Al concentrations. The crystal structures of ZnO and α-Al_2O_3 are not the same, so lattice parameters have been modelled by considering how the average bond length will change as Al is substituted onto the Zn lattice. This model is given in Eq. (8).

$$c(x) = c_{ZnO} + x\frac{\Delta b}{u} \tag{8}$$

where c_{ZnO} is the lattice parameter c of pure ZnO, Δb is the difference in

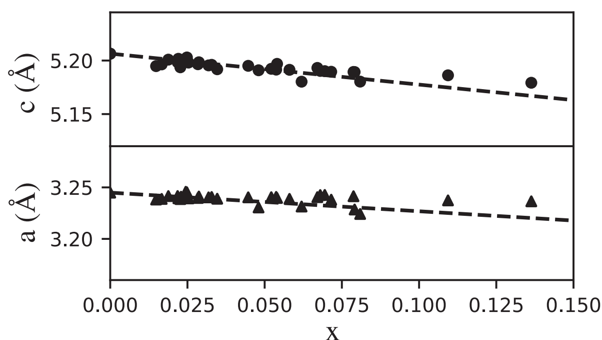

Fig. 4. The lattice parameters of AZO decreased as the Al concentration increased. The dashed lines represent the expected lattice changes calculated from established ionic and covalent bond lengths.

bond length between the Al-O and the Zn-O bonds. u is the ratio of the bond length to the c parameter. A similar expression can de derived for the lattice parameter a. The bond length, *b*, for Zn-O can be estimated using the ionic radii of Zn^{2+}, and O^{2-}, which are 0.74 Å and 1.24 Å, respectively. [39]. The Al-O bond is more covalent in nature, and should therefore be estimated using the covalent radii of Al^{3+} and O^{2-}, which are 1.21 Å and 0.66 Å, respectively. [40] Δb for the Al-Zn-O system was calculated to be -0.289 Å. The measured value of *c* for pure ZnO was 5.207 Å, which resulted in a *u*-value of 0.380. This is close to the established value of 0.382 for ZnO. [41] Fig. 4 demonstrates a good agreement between the measured lattice parameters and the model provided in Eq. (8), resulting in an R^2 value of 0.73. Both the a and c lattice parameters are slightly bigger than the model at higher Al concentrations. This could be an indication that the sputtering efficiencies during SIMS measurements were higher for these samples. The sputtering efficiency may have been increased by higher concentrations of grain boundaries and by matrix effects due to higher Al concentrations. However, the strong correlation between the XRD measurements and the Al concentrations as measured by SIMS, supports the reliability of the SIMS measurements at concentrations below $x = 0.08$. Because of this it is reasonable to conclude that most of the Al atoms are incorporated onto the Zn lattice at these concentrations.

3.3. Electrical and optical properties

Al incorporation increased the conductivity of the samples. The charge carrier concentration of AZO was typically around 5×10^{20} cm^{-3}, with Hall mobilities ranging from 5.9 cm^2/Vs to 24 cm^2/Vs. The minimum resistivity was from 5.9×10^{-4} ohm cm.

Fig. 5 shows a typical transmission measurements of AZO. The transparency at visible wavelengths is in the range of 85–95%. There is a single transition at around 3.3 eV, which roughly corresponds to the expected band edge absorption in ZnO. A corresponding absorption in AZO occurs closer to 4 eV. The higher energy is probably due to a Burstein-Moss shift caused by the high carrier concentration. Absorption below 1 eV in AZO is likely due to free carrier absorption.

3.4. Growth conditions and Al incorporation

Eq. (2) suggests that the oxygen balance, O/Zn, can be changed by both the tBuOH flow rate, F_{tBuOH}, and by the total MO flow, F^{MO}_{TOT}. Fig. 6 displays how incorporation efficiency, *k*, depends on O/Zn as it is

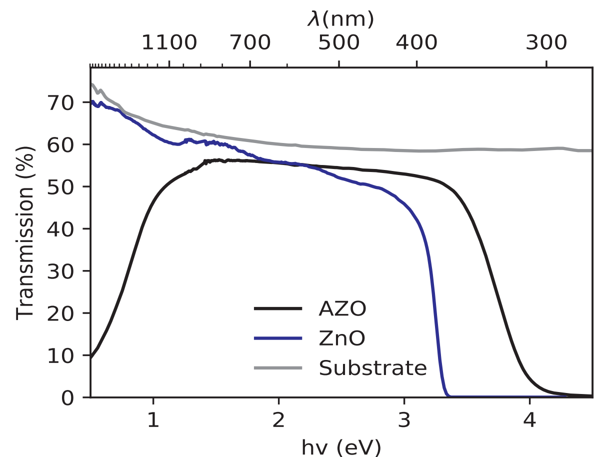

Fig. 5. Transmission measurements of pure ZnO (blue), AZO (black), and substrate(grey). The transmission though AZO in the visible region is roughly 85%. ZnO shows a single transition corresponding to the band absorption of ZnO. AZO shows a blue shifted absorption edge as well as free carrier absorption below 1 eV.) (For interpretation of the references to color in this figure legend, the reader is referred to the web version of this article.)

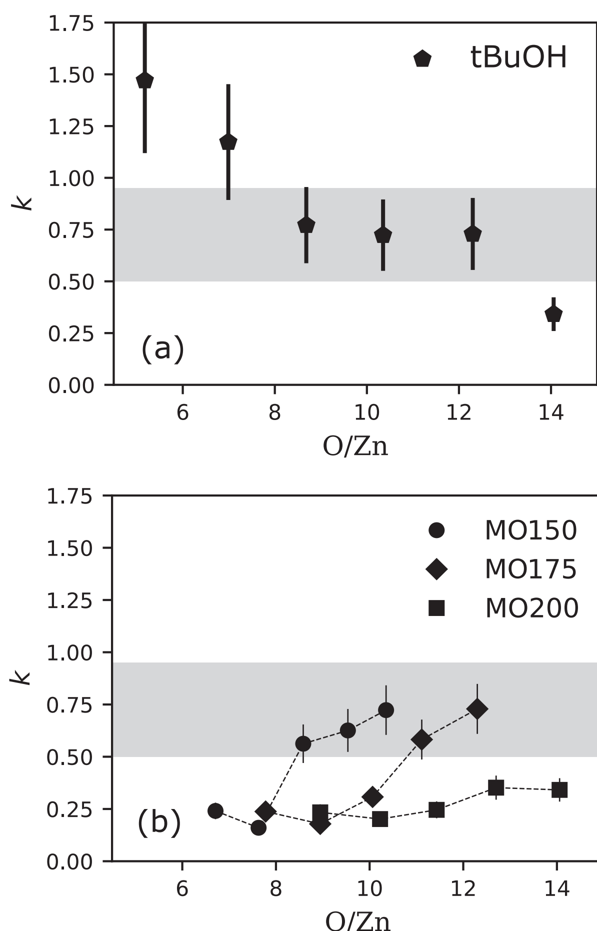

Fig. 6. The figure shows the relationship between incorporation efficiency, k, and the O/Zn balance as changed by varying F_{tBuOH} and F^{MO}_{TOT}. (a) At a constant F^{MO}_{TOT} of 5500sccm, incorporation decreases with O/Zn as F_{tBuOH} increases. (b) Increasing O/Zn by F^{MO}_{TOT}, leads to an increased incorporation. The rate of increase in (b) is dependent on F_{tBuOH}. The incorporation efficiency can be divided into separate regimes as marked by the grey area.

changed by each of these flow parameters. In Fig. 6a, $k > 1$ when O/Zn <8. However, when $8 < O/Zn < 13$, k remains at around 0.75. Then k drops to 0.30 for O/Zn>13. These results show that when the tBuOH flow is changed, the increase in O/Zn is correlated with a decreased Al incorporation efficiency. In Fig. 6b, $0.20 < k < 0.30$ for low O/Zn. As O/Zn increases, MO150 and MO175 demonstrate a sharp transition to $k > 0.50$. However, the rate of change decreases as the tBuOH flow rate increases from 150 to 200 sccm. For MO200, there is no comparable increase. These results show that when the total MO flow is changed, the increase in O/Zn is correlated with an increased Al incorporation. Fig. 6a and b show opposing trends with respect to O/Zn, however, the values of k cluster about $0.20 < k < 0.30$ or $0.5 < k < 0.75$. The clustering of k values indicates that incorporation is affected by separate mechanisms. $k > 1$ for low O/Zn in Fig. 6a may also present a third incorporation regime. The deposition rate (not shown) for these samples is constant at 0.07 ± 0.02 nm/s. This rate corresponds to growth rates from similar techniques and temperatures [21,26,42].

Fig. 7 shows how the incorporation efficiency is affected by increasing the total volumetric flow rate, F^{MO}_{TOT}, through the MO injector. It is important to note that while the volumetric flow rates through the MO injector were changed, the molar flow rates were kept constant. The two incorporation regimes are illustrated by the dotted lines and the incorporation efficiencies for the tBuOH and TMAl series are also indicated. All k values are shown to follow the dotted lines closely. MO150, MO175, and MO200 have low k values when, F^{MO}_{TOT}, was below

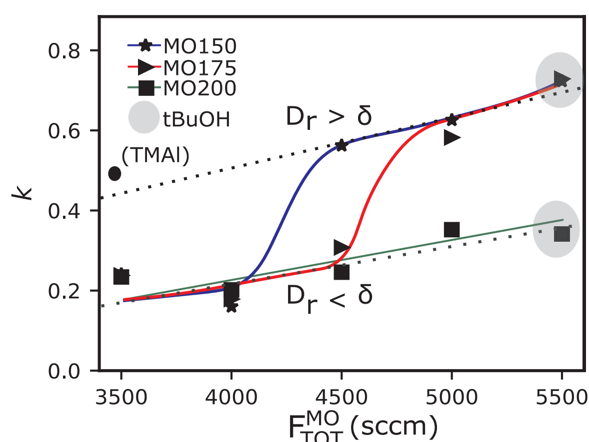

Fig. 7. Incorporation efficiency, k, as a function of the total flow, F^{TOT}_{MO}, through the MO injector. F^{TOT}_{MO} is increased by the MO carrier flow rate, which dilutes the flows coming from the MO bubblers. The flow rates used are listed in Table 1. This process is repeated with constant tBuOH flow rates of 150, 175, and 200 sccm, labelled MO150, MO175, and MO200, respectively. The incorporation efficiency is divided into two regimes, and the blue, red, and green eye-guides show how tBuOH flow affects the transition from lower to upper incorporation regimes for MO150, MO175, and MO200 respectively. (For interpretation of the references to color in this figure legend, the reader is referred to the web version of this article.)

4000 sccm. MO150 demonstrates a sharp increase in incorporation efficiency when F^{MO}_{TOT} is between 4000 and 4500 sccm. A similar behaviour is observed also for MO175, where the transition occurs when F^{MO}_{TOT} is between 4500 and 5000 sccm. However, the incorporation for the MO200 samples remains in the lower regime for all values of F^{MO}_{TOT}. This sudden change to a higher incorporation efficiency reflects transitions between incorporation regimes when when F^{MO}_{TOT} reaches a critical flow rate. The shift in the transition suggests that the value of the critical flow rate depends on the O/Zn balance as given by the tBuOH flow rate.

Figs. 6 and 7 suggest that both the oxygen balance (O/Zn) and the total flow rate affect the incorporation efficiency of Al during AZO growth by MOCVD. The sensitivity of the system to one parameter seems to depend on the value of the other. Below we suggest some mechanisms to help explain how incorporation efficiency is linked to both O/Zn and volumetric flow rates. Al is incorporated at the growth interface through physisorption and/or chemisorption of Al precursors. The mobility and reactivity of the Al precursors on the growth surface are determined by their chemical character, which depends on the reactions that they have gone through in the gas boundary layer. Separate Al incorporation regimes could therefore be explained in terms of how growth conditions affect the reactions of the Al precursors in the boundary layer, and the reactivity of the Al precursors that eventually reach the growth surface. At 370 °C, tBuOH has already started to decompose into H_2O and isobutene. [34] TMAl will therefore be in the presence of both tBuOH and H_2O, as well as DEZn and zinc alkoxide. TMAl is a strong Lewis acid and is extremely reactive to oxygen precursors due to an unfilled p-orbital on the Al atom. [43] Oxygen can form very stable bonds with Al, and thereby lower the reactivity of the Al precursors. Oxidation of TMAl is therefore a common source of oxygen contamination in the production of AlGaAs, [44] and the proposed reaction of TMAl is similar to Eq. (9).

$$AlMe_3(g) + nROH(g) \rightarrow Me_{3-n}Al(OR)_n(g) + R_{waste}(g) \quad (9)$$

where R = tBu ($C(CH_3)_3$), H, or Me (CH_3). R_{waste} consists of methane (CH_4) or some other organic molecule corresponding to Me-tBu, but the exact nature is not important for our discussion. n in Eq. (9) is related to the completeness of the reaction. It can be thought of as the degree of oxidation, or the number of Al-O bonds formed on the Al precursor, and

can take a value between 0 and 3. According to the reaction in Eqs. (6) and (9), the growth surface is likely to be terminated in |–OR, where R = tBu or H. The presence of a methyl group on the Al precursors facilitates for chemisorption on the growth interface as the methyl group is eliminated to form Al-O bonds with the surface. The direct reaction between TMAl and a |-Zn-OH terminated surface has been studied in the context of ALD, where TMAl tends to etch away Zn from the surface through exchange reactions. [45] Similar exchange reactions during MOCVD growth could contribute to incorporation efficiencies higher than unity. TMAl would be able to reach the growth interface either when the O/Zn balance is very low, or when the boundary layer is very thin. This might help explain the that $k > 1$ for samples with low O/Zn in Fig. 6. Thus the reactivities of the Al precursors in Eq. (9) can be ordered according to the degree of oxidation so that: $Al(OR)_3 < Al(CH_3)(OR)_2 < Al(CH_3)_2(OR) < Al(CH_3)_3$, where R = tBu or H.

In the incorporation regime where $0.5 < k < 0.75$, as marked by the grey section in Fig. 6, Al incorporation occurs mainly through $(CH_3)_{3-n}$-Al-$(OtBu)_n$ with $n < 3$. These molecules are still very reactive because demethylation of the Al precursors at the surface is possible, but the probability of this reaction is lowered by the partial oxidation. $n < 3$ is possible if the boundary layer is thin, and the O/Zn values are too low for the oxidation reaction between TMAl and tBuOH (or H_2O) to reach equilibrium before the Al precursors arrived at the growth surface.

In the regime where $k < 0.3$, Eq. (9) has been able to run to completion, so that $n = 3$. Under these circumstances incorporation occurs through the physisorption of $Al(OR)_3$, where R = H or OtBu. $Al(OH)_3$ can physisorb, but is unlikely to decompose further at an -OR terminated surface. However, $Al(OtBu)_3$ is more likely to decompose through a process similar to that of zinc alkoxides. [33] This is a less likely process and would have a lower reactivity, resulting in a lower incorporation efficiency. $Al(OR)_3$ will form if the O/Zn is sufficiently high and the boundary layer is sufficiently thick to allow for a complete reaction.

The effects of volumetric flow on incorporation demonstrated in Fig. 7 could be explained by considering the effect of volumetric flow on the boundary layer. Increasing the volumetric flow rate results in a higher flow velocity through the injector. Modelling of fluid dynamics in a vertical MOCVD reactor suggests that the thickness of the diffusion boundary layer is proportional to $1/\sqrt{v}$, where v is the flow velocity. [46] An increase of volumetric flow of an incompressible medium from 3500 to 5500 sccm would decrease the boundary layer by about 20%. However, flow velocities approaches the limit boundary for compressible flows, and the exact relationship between the volumetric flow rates and the flow velocities depend on the geometry and dimensions of the flow system, which are not available.

The effects of O/Zn and boundary layer can be combined into the idea of a reaction depth of Al precursors. Fig. 8 illustrates the concept of the reaction depth, D_r, defined as the depth into the diffusion boundary layer where a significant portion of Al precursors still retain a methyl group. That is, the depth beyond which all the Al precursors are completely oxidized, $Al(OR)_3$ with R = tBu or H. Fig. 8 also illustrates how the relationship between the boundary layer thickness, δ, and D_r, determines which Al precursors will be able to reach the growth interface. The most reactive Al precursor able to reach the growth interface for different combinations of δ and D_r are $Al(OR)_3$, $Al(OR)Me_2$, or TMAl for $D_r < \delta$, $D_r > \delta$, and $D_r > > \delta$, respectively. The value of D_r is a function of the O/Zn balance because a higher concentration of oxygen precursors will lower D_r by increasing the probability of oxidation reactions. Thus the trends observed in Fig. 7 can be explained in terms of the relation between δ and D_r as follows. Low incorporation for low total flow, indicates that $D_r < \delta$, and incorporation must have occurred through the decomposition of $Al(OtBu)_3$, which is less effective. However, as flow rates increased, and the boundary layer became thinner than D_r, and $Al(OR)_nCH_{3-n}$ with $n < 3$ were able to break through the boundary layer and reach the surface, leading to more effective incorporation. This explains the transition from lower to higher incorporation as flow rates increased.

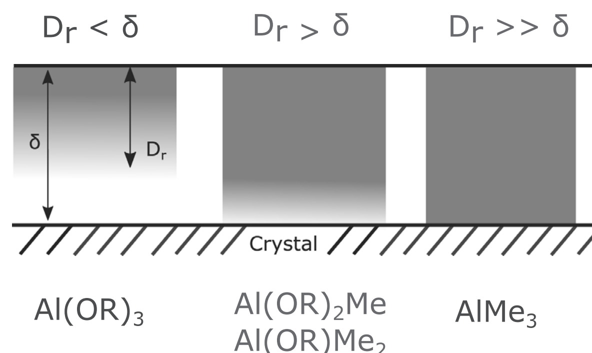

Fig. 8. The figure shows a qualitative model showing the idea of a reaction depth, D_r. The type of Al precursor at the growth interface depends on how deeply methylated Al precursors is able to penetrate into the boundary layer before losing their methyl group through oxidation. The Al precursors at the surface therefore depends on the O/Zn balance and the boundary layer thickness, δ. The most reactive Al precursors reaching the surface in each incorporation regime are also indicated.

Increasing the tBuOH molar flow causes a higher O/Zn balance in the boundary layer, and thereby lowers the value of D_r. Therefore, a higher flow rate is needed to cause a corresponding decrease in δ. Thus as the tBuOH flow increased from 150 to 175 sccm, the total MO flow rates necessary to make the transition increased from 4000 to 4500 sccm. This also explains why MO200 remained in the lower incorporation regime, as the higher oxygen content caused $D_r < \delta$ for F^{MO}_{TOT} values between 3500 and 5500 sccm. It is expected that a transition could occur at a higher total flow rates, which would lower the boundary layer thickness further. While these observation provide a qualitative insight, further investigations would be necessary for a quantitative characterisation of these processes. Fluid dynamics simulations would prove especially useful. However, awareness of these mechanisms may prove important for further developments of impurity incorporations through MOCVD processes of similar reactor designs, particularly for the growth of AZO.

4. Conclusions

Several series of AZO thin films have been grown on c-oriented sapphire substrates. SIMS measurements showed that the Al content reached as high as 14% (6×10^{21} cm^{-3}). XRD measurements showed that the wurtzite structure of ZnO was maintained, while the lattice parameters changed from 5.207 Å (pure ZnO) to 5.181 Å in a predictable manner. These results indicate that most of the Al was incorporated on the Zn lattice. Increasing O/Zn by adding more tBuOH decreased the Al incorporation, while increasing O/Zn by increasing the total volumetric flow had the opposite effect. This suggested that incorporation is determined both by the O/Zn balance and the boundary layer thickness. The incorporation efficiencies were also clustered about three separate regimes.

The incorporation regimes have been discussed in terms of the Al precursors available to react at the growth interface. The idea of a reaction depth was introduced to describe the maximum depth into the boundary layer before the Al precursors less reactive as all the methyl groups were lost through oxidation. The transition between the incorporation regimes has been explained by how the reaction depth of the Al precursor compares to the boundary layer thickness, as the relation between the two determine which Al precursors are able to reach the growth interface. These discussions may contribute to the understanding of MOCVD growth of AZO by illustrating how the incorporation efficiency of Al is affected by precursors chemistry, oxygen balance and flow configurations. They also suggest that the O/Zn balance and boundary layer thickness provide some level of control over the

prereactions of the precursors within the boundary layer, which should be relevant for other systems as well.

Declaration of Competing Interest

The authors declare that they have no known competing financial interests or personal relationships that could have appeared to influence the work reported in this paper.

Acknowledgements

We acknowledge fruitful discussions with Øystein Prytz, Augustinas Galeckas and Christian Zimmermann. This work was supported by the Faculty of Mathematics and Natural Sciences via the strategic research program FOXHOUND. We also want to acknowledge financial support provided by the Ministry of Education, Norway. The Research Council of Norway is acknowledged for the support to the Norwegian Micro- and Nano- fabrication facility, NorFab (245963/F50) and the Norwegian Ph.D. Network on Nanotechnology for Microsystems, Nano-Network (221860/F40).

References

[1] A. Kumar Rana, D.-K. Ban, M. Patel, J.-H. Yun, J. Kim, A transparent photovoltaic device based on Cu2O/ZnO/AZO for see-through applications, Mater. Lett. 255 (2019) 126517, https://doi.org/10.1016/j.matlet.2019.126517.

[2] R.N. Chauhan, C. Singh, R.S. Anand, J. Kumar, Thickness-dependent structural, optical, and electrical characteristics of ZnO:Al thin films and application in OLEDs, IEEE Trans. Electron Devices 61 (11) (2014) 3775–3782, https://doi.org/10.1109/TED.2014.2353300.

[3] H. Liu, V. Avrutin, N. Izyumskaya, Ü. Özgür, H. Morkoç, Transparent conducting oxides for electrode applications in light emitting and absorbing devices, Superlattices Microstruct. 48 (5) (2010) 458–484, https://doi.org/10.1016/j.spmi.2010.08.011.

[4] T. Minami, Transparent conducting oxide semiconductors for transparent electrodes, Semicond. Sci. Technol. 20 (4) (2005) S35–S44, https://doi.org/10.1088/0268-1242/20/4/004.

[5] F.M. Simanjuntak, D. Panda, T.L. Tsai, C.A. Lin, K.H. Wei, T.Y. Tseng, Enhancing the memory window of AZO/ZnO/ITO transparent resistive switching devices by modulating the oxygen vacancy concentration of the top electrode, J. Mater. Sci. 50 (21) (2015) 6961–6969, https://doi.org/10.1007/s10853-015-9247-y.

[6] R. Mundle, C. Carvajal, A.K. Pradhan, ZnO/Al:ZnO Transparent resistive switching devices grown by atomic layer deposition for memristor applications, Langmuir 32 (19) (2016) 4983–4995, https://doi.org/10.1021/acs.langmuir.6b01014.

[7] N. Kinsey, C. DeVault, J. Kim, M. Ferrera, V.M. Shalaev, A. Boltasseva, Epsilon-near-zero Al-doped ZnO for ultrafast switching at telecom wavelengths, Optica 2 (7) (2015) 616, https://doi.org/10.1364/optica.2.000616.

[8] P. Novák, Possibilities of increasing the usability of sputtered AZO films as a transparent electrode, Phys. Status Solidi Appl. Mater. Sci. 216 (7) (2019) 1800814, https://doi.org/10.1002/pssa.201800814.

[9] T. Minami, H. Nanto, S. Takata, Highly conductive and transparent aluminum doped zinc oxide thin films prepared by RF magnetron sputtering, Jpn. J. Appl. Phys. 23 (Part 2, No. 1) (1984) L280–L282, https://doi.org/10.1143/JJAP.23.L280.

[10] B.E. Sernelius, K.F. Berggren, Z.C. Jin, I. Hamberg, C.G. Granqvist, Band-gap tailoring of ZnO by means of heavy Al doping, Phys. Rev. B 37 (17) (1988) 10244–10248, https://doi.org/10.1103/PhysRevB.37.10244.

[11] C.Y. Liu, F. He, Y.F. Zhang, S.G. Zang, Y. Zuo, J.R. Ma, Effect of oxygen partial pressure on properties of ZnO/Al thin films prepared by pulsed dc reactive magnetron sputtering with SpeedFlo controller, Mater. Technol. 30 (4) (2015) 249–256, https://doi.org/10.1179/1753555715Y.0000000001.

[12] H. Hung-Chun Lai, T. Basheer, V.L. Kuznetsov, R.G. Egdell, R.M.J. Jacobs, M. Pepper, P.P. Edwards, Dopant-induced bandgap shift in Al-doped ZnO thin films prepared by spray pyrolysis, J. Appl. Phys. 112 (8) (2012) 083708, https://doi.org/10.1063/1.4759208.

[13] A. Nakrela, N. Benramdane, A. Bouzidi, Z. Kebbab, M. Medles, C. Mathieu, Site location of Al-dopant in ZnO lattice by exploiting the structural and optical characterisation of ZnO: Al thin films, Results Phys. 6 (2016) 133–138, https://doi.org/10.1016/j.rinp.2016.01.010.

[14] P.J. Cao, S. Han, W.J. Liu, F. Jia, Y.X. Zeng, D.L. Zhu, Y.M. Lu, Effect of oxygen flowrate on optical and electrical properties in Al doped ZnO thin films, Mater. Technol. 29 (6) (2014) 336–340, https://doi.org/10.1179/1753555714Y.0000000172.

[15] T. Coman, E.L. Ursu, V. Nica, V. Tiron, M. Olaru, C. Cotofana, M. Dobromir, A. Coroaba, O.-G.G. Dragos, N. Lupu, O.F. Caltun, C. Ursu, Improving the uncommon (110) growing orientation of Al-doped ZnO thin films through sequential pulsed laser deposition, Thin Solid Films 571 (P1) (2014) 198–205, https://doi.org/10.1016/j.tsf.2014.10.037.

[16] S.M. Park, T. Ikegami, K. Ebihara, P.K. Shin, Structure and properties of transparent conductive doped ZnO films by pulsed laser deposition, Appl. Surf. Sci. 253 (3) (2006) 1522–1527, https://doi.org/10.1016/j.apsusc.2006.02.046.

[17] N.P. Dasgupta, S. Neubert, W. Lee, O. Trejo, J.-R. Lee, F.B. Prinz, Atomic layer deposition of Al-doped ZnO films: effect of grain orientation on conductivity, Chem. Mater. 22 (16) (2010) 4769–4775, https://doi.org/10.1021/cm101227h.

[18] D.-J. Lee, H.-M. Kim, J.-Y. Kwon, H. Choi, S.-H. Kim, K.-B. Kim, Structural and electrical properties of atomic layer deposited Al-doped ZnO films, Adv. Funct. Mater. 21 (3) (2011) 448–455, https://doi.org/10.1002/adfm.201001342.

[19] T. Tynell, H. Yamauchi, M. Karppinen, R. Okazaki, I. Terasaki, Atomic layer deposition of Al-doped ZnO thin films, J. Vac. Sci. Technol. A Vacuum, Surfaces, Film. 31 (1) (2012) 01A109, https://doi.org/10.1116/1.4757764.

[20] J.W. Elam, S.M. George, Growth of ZnO/Al 2 O 3 alloy films using atomic layer deposition techniques, Chem. Mater. 15 (19) (2003) 1020–1028, https://doi.org/10.1021/cm020607+.

[21] J. Hu, R.G. Gordon, Textured aluminumdoped zinc oxide thin films from atmospheric pressure chemicalvapor deposition, J. Appl. Phys. 71 (2) (1992) 880–890, https://doi.org/10.1063/1.351309.

[22] S. Kuprenaite, A. Abrutis, V. Plausinaitiene, A. Arkhangelskiy, V. Kubilius, L. Silimavicius, T. Murauskas, Z. Saltyte, Properties of Al-doped ZnO films grown by atmospheric pressure MOCVD on different orientation sapphire substrates, Integr. Ferroelectr. 173 (1) (2016) 128–139, https://doi.org/10.1080/10584587.2016.1186440.

[23] S. Brochen, M. Lafossas, I.-C. Robin, P. Ferret, F. Gemain, J. Pernot, G. Feuillet, Residual and intentional n-type doping of ZnO thin films grown by metal-organic vapor phase epitaxy on sapphire and ZnO substrates, J. Appl. Phys. 115 (11) (2014) 113508, https://doi.org/10.1063/1.4868591.

[24] J.G. Lu, S. Fujita, T. Kawaharamura, H. Nishinaka, Y. Kamada, T. Ohshima, Z.Z. Ye, Y.J. Zeng, Y.Z. Zhang, L.P. Zhu, H.P. He, B.H. Zhao, Carrier concentration dependence of band gap shift in n-type ZnO:Al films, J. Appl. Phys. 101 (8) (2007) 083705, https://doi.org/10.1063/1.2721374.

[25] S. Oda, H. Tokunaga, N. Kitajima, J.I. Hanna, I. Shimizu, H. Kokado, Highly oriented zno films prepared by MOCVD from diethylzinc and alcohols, Jpn. J. Appl. Phys. 24 (12 R) (1985) 1607–1610, https://doi.org/10.1143/JJAP.24.1607.

[26] D. Lamb, S. Irvine, Growth properties of thin film ZnO deposited by MOCVD with n-butyl alcohol as the oxygen precursor, J. Cryst. Growth 273 (1-2) (2004) 111–117, https://doi.org/10.1016/j.jcrysgro.2004.08.027.

[27] J. van Deelen, A. Illiberi, B. Kniknie, H. Steijvers, A. Lankhorst, P. Simons, APCVD of ZnO:Al, insight and control by modeling, Surf. Coatings Technol. 230 (2013) 239–244, https://doi.org/10.1016/j.surfcoat.2013.06.055.

[28] A. Illiberi, P. Simons, B. Kniknie, J. van Deelen, M. Theelen, M. Zeman, M. Tijssen, W. Zijlmans, H. Steijvers, D. Habets, A. Janssen, E. Beckers, Growth of ZnOx:Al by high-throughput CVD at atmospheric pressure, J. Cryst. Growth 347 (1) (2012) 56–61, https://doi.org/10.1016/j.jcrysgro.2012.03.007.

[29] A. Illiberi, B. Kniknie, J. van Deelen, H. Steijvers, D. Habets, P. Simons, A. Janssen, E. Beckers, Industrial high-rate (4nm/s) deposition of low resistive and transparent ZnOx:Al films on glass, Sol. Energy Mater. Sol. Cells 95 (7) (2011) 1955–1959, https://doi.org/10.1016/j.solmat.2011.01.007.

[30] A. Illiberi, R. Scherpenborg, Y. Wu, F. Roozeboom, P. Poodt, Spatial atmospheric atomic layer deposition of Al x Zn 1 x O, ACS Appl. Mater. Interfaces 5 (24) (2013) 13124–13128, https://doi.org/10.1021/am404137e.

[31] V. Venkatachalapathy, A. Galeckas, A. Zubiaga, F. Tuomisto, A.Y. Kuznetsov, Changing vacancy balance in ZnO by tuning synthesis between zinc/oxygen lean conditions, J. Appl. Phys. 108 (4) (2010) 046101, https://doi.org/10.1063/1.3462394.

[32] H. Huang, W.Y. Jiang, S.P. Watkins, Flow modulation epitaxy of ZnO films on sapphire substrates, J. Cryst. Growth 310 (18) (2008) 4050–4053, https://doi.org/10.1016/j.jcrysgro.2008.06.073.

[33] A.C. Jones, S.A. Rushworth, J. Auld, Recent developments in metalorganic precursors for metalorganic chemical vapour deposition, J. Cryst. Growth 146 (1-4) (1995) 503–510, https://doi.org/10.1016/0022-0248(94)00469-2.

[34] C. Thiandoume, V. Sallet, R. Triboulet, O. Gorochov, Decomposition kinetics of tertiarybutanol and diethylzinc used as precursor sources for the growth of ZnO, J. Cryst. Growth 311 (5) (2009) 1411–1415, https://doi.org/10.1016/j.jcrysgro.2008.12.036.

[35] U. Holzwarth, N. Gibson, The Scherrer equation versus the 'Debye-Scherrer equation', Nat. Nanotechnol. 6 (9) (2011), https://doi.org/10.1038/nnano.2011.145. 534–534

[36] J. Greene, S. Barnett, A. Rockett, G. Bajor, Modeling of dopant incorporation, segregation, and ion/surface interaction effects during semiconductor film growth by molecular beam epitaxy and plasma-based techniques, Appl. Surf. Sci. 22-23 (PART 2) (1985) 520–544, https://doi.org/10.1016/0378-5963(85)90184-9.

[37] G.B. Stringfellow, Thermodynamic aspects of organometallic vapor phase epitaxy*, J. Cryst. Growth 62 (1983) 225–229.

[38] S. Yoshioka, F. Oba, R. Huang, I. Tanaka, T. Mizoguchi, T. Yamamoto, Atomic structures of supersaturated ZnOAl2O3 solid solutions, J. Appl. Phys. 103 (1) (2008) 014309, https://doi.org/10.1063/1.2829785.

[39] R.D. Shannon, Revised effective ionic radii and systematic studies of interatomic distances in halides and chalcogenides, Acta Crystallogr. Sect. A 32 (5) (1976) 751–767, https://doi.org/10.1107/S0567739476001551.

[40] B. Cordero, V. Gómez, A.E. Platero-Prats, M. Revés, J. Echeverría, E. Cremades, F. Barragán, S. Alvarez, Covalent radii revisited, J. Chem. Soc. Dalt. Trans. 0 (21) (2008) 2832–2838, https://doi.org/10.1039/b801115j.

[41] E.H. Kisi, M.M. Elcombe, u parameters for the wurtzite structure of ZnS and ZnO using powder neutron diffraction, Acta Crystallogr. Sect. C Cryst. Struct. Commun. 45 (12) (1989) 1867–1870, https://doi.org/10.1107/S0108270189004269.

[42] A. Illiberi, P. Poodt, P.J. Bolt, F. Roozeboom, Recent advances in atmospheric

vapor-phase deposition of transparent and conductive zinc oxide, Chem. Vap. Depos. 20 (7-9) (2014) 234–242, https://doi.org/10.1002/cvde.201400056.
[43] H.M. Nguyen, H.Y. Tang, W.F. Huang, M.C. Lin, Mechanisms for reactions of trimethylaluminum with molecular oxygen and water, Comput. Theor. Chem. 1035 (2014) 39–43, https://doi.org/10.1016/j.comptc.2014.02.015.
[44] S. Yamashita, K. Watanuki, H. Ishii, Y. Shiba, M. Kitano, Y. Shirai, S. Sugawa, T. Ohmi, Dependence of the decomposition of trimethylaluminum on oxygen concentration, J. Electrochem. Soc. 158 (2) (2011) H93, https://doi.org/10.1149/1.3517080.
[45] J. Elam, Z. Sechrist, S. George, ZnO/Al2O3 nanolaminates fabricated by atomic layer deposition: growth and surface roughness measurements, Thin Solid Films 414 (1) (2002) 43–55, https://doi.org/10.1016/S0040-6090(02)00427-3.
[46] N. Shibata, S. Zembutsu, A boundary layer model for the MOCVD process in a vertical cylinder reactor, Jpn. J. Appl. Phys. 26 (9R) (1987) 1416–1421, https://doi.org/10.1143/JJAP.26.1416.